A paraboloidal electrostatic reflector for molecular-beam time-of-flight photoelectron spectrometers

Jhobe Steadman[a] and Jack A. Syage[b]
The Aerospace Corporation, P. O. Box 92957/M5-754, Los Angeles, California 90009

(Received 6 July 1993; accepted for publication 9 August 1993)

We describe a design for a paraboloidal electrostatic reflector (PER) adapted for molecular-beam time-of-flight (TOF) photoelectron spectrometers. The PER offers a nearly two orders of magnitude improvement in detection efficiency over standard line-of-sight TOF detection. The energy resolution $\Delta E/E$ is nominally about 0.02, but can be improved to about 0.005 (to a current limit of $\Delta E = 10$ meV) at some expense in sensitivity. The PER makes possible sensitive measurements for inherently weak ionization experiments. We have used our spectrometer in applications involving low-power picosecond pulses, low-density molecular clusters, and ionization through dissociative states.

I. INTRODUCTION

Resonance-enhanced multiphoton ionization photoelectron spectroscopy (REMPI/PES) is a powerful method for studying excited-state dynamics of molecules.[1] However, electron detection by standard time-of-flight (TOF) or energy-dispersive analyzers is limited by low collection efficiency. High laser intensities are often used to compensate for this deficiency, but this can lead to undesirable complications (e.g., space-charge repulsion). Trevor, Van Woerkom, and Freeman (TVF) recently reported on a device they call a parabolic mirror analyzer that achieves a large solid angle of detection in a TOF device.[2] A similar concept was also reported by Liu *et al.*[3] We report on a related device for use with a molecular-beam apparatus and describe operating features to improve sensitivity and resolution.

Our paraboloidal electrostatic reflector (PER) is based on the design by TVF and consists of two concentric slightly separated paraboloidally shaped grids.[2] A reflecting field for electrons ejected off-axis from the TOF drift tube is created by applying, respectively, a ground and negative potential to the inner- and outer-grid structure. Reflected electrons that originate from the focus of the paraboloid travel collimated paths of equal length to the detector. The PER, therefore, is ideally suited for TOF measurements of electron kinetic energy. Whereas TVF designed a PER for studies of above-threshold ionization processes in a static atomic gas, we have incorporated the PER into a pulsed molecular-beam apparatus in order to study molecular excited-state dynamics. Our spectrometer also incorporates a reflectron-type mass spectrometer in the source chamber that potentially allows us to monitor ion mass spectra and photoelectron spectra concurrently.

An alternative method for obtaining high collection efficiency in a time-of-flight configuration is to use magnetic field collimation (e.g., a magnetic-bottle spectrometer).[4] However, compared to the PER approach, the magnetic bottle does not preserve the angular information for ionization, subjects the excitation volume to high magnetic fields, and involves a relatively complex design. Zero-kinetic-energy (ZEKE) photoelectron spectroscopy offers high sensitivity and high resolution, but requires two tunable laser sources, one to excite an intermediate resonance and the other to excite ion vibronic thresholds to give near zero-kinetic-energy electrons (or actually field ionized very high n Rydberg states).[5] Furthermore, ZEKE detects one ion state at a time, as opposed to the TOF method, which records an entire ion spectrum, though at lower-energy resolution.

The fabrication of the paraboloidal grids is a critical step in the construction of the spectrometer. TVF made their grids from mesh material using electrochemical etching followed by electrochemical plating. We had difficulty achieving uniform quality over the entire grid forms by this method. We instead developed a procedure that uses chemical etching and electrodeless chemical plating. This method is reliable and suitable for in-house fabrication.

We have applied the PER/TOF photoelectron spectrometer to a number of inherently weak ionization experiments involving (1) low-energy picosecond pulses, (2) low-density molecular clusters, including the use of picosecond ionization,[6,7] and (3) low-efficiency ionization through dissociative states. The advantages of improved electron collection efficiency could advance the use of time-resolved photoelectron spectroscopy, for which there are currently very few facilities.[7–12] Other applications are also suggested.

II. EXPERIMENT

A. Molecular-beam system

A schematic of the molecular-beam photoelectron spectrometer is illustrated in Fig. 1. The apparatus consists of a source chamber and a photoelectron chamber made from a stainless cross and tee, respectively (8-in.-diam tube, 10-in.-diam conflat flanges). A double-sided stainless-steel flange joins the two chambers. Optical ports allow the laser beam to pass into the source chamber immediately in front of the pulsed valve for mass spectrometric studies or

[a]Current address: GeoCenters Inc., Gun Powder Branch, P.O. Box 68, Aberdeen Proving Grounds, MD 21010.
[b]Author to whom correspondence should be addressed.

 0034-6748/93/64(11)/3094/10/$6.00

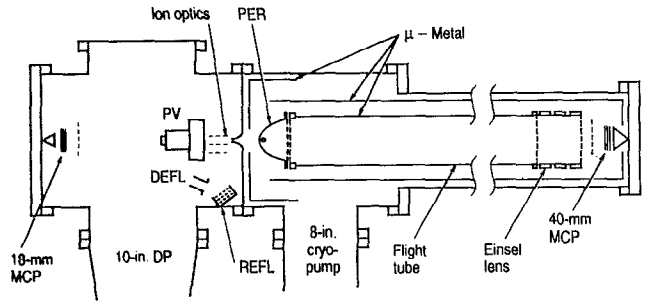

FIG. 1. Experimental schematic of the molecular-beam photoelectron spectrometer. Terms are defined as follows: DEFL, deflector plates; DP, diffusion pump; MCP, microchannel plate detector; PER, paraboloidal electrostatic reflector; PV, pulsed valve; REFL, reflecting grids. A water-cooled baffle for the DP, and gate valves for the DP and cryopump, are not shown.

into the experimental chamber through the parabolic mirror assembly for photoelectron spectroscopy studies. The source chamber is pumped by a 10-in. diffusion pump. In order to suppress backstreaming of diffusion pump oil, a baffle above the diffusion pump is maintained at 5 °C by circulating chilled water through the trap. The experimental chamber is pumped by an 8-in. cryopump. The diffusion pump and cryopump are each equipped with a gate valve.

The apparatus is equipped with a temperature-controlled pulsed valve of a design described before.[13] Typical operating conditions are 10–25 psi Ar backing pressure, 500–750-μm nozzle aperture, 200–300 μs pulse width, 4-cm nozzle-skimmer distance, and 1-mm-diam skimmer. Typical chamber pressures at 10-Hz operation are $5–10\times10^{-6}$ and $5–20\times10^{-8}$ Torr for the source and photoelectron chambers, rising from base pressures of 4×10^{-7} and 3×10^{-8} Torr, respectively.

B. Source chamber mass spectrometer

The pulsed valve is mounted directly to the double-sided stainless-steel flange which separates the chambers. In order to extract ions perpendicular to the molecular-beam direction, electrostatic lenses are mounted to the face

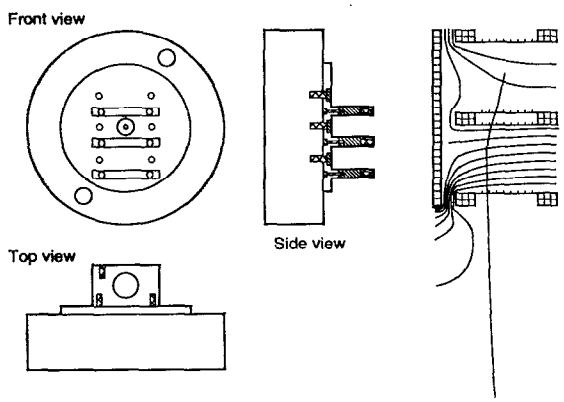

FIG. 2. Schematic of source-chamber mass spectrometer ion optics and SIMION calculation of ion trajectories for typically operating conditions. The grid voltages from top to bottom are 200, 170, and 0 V, respectively, and the isolated disk plate is at 140 V.

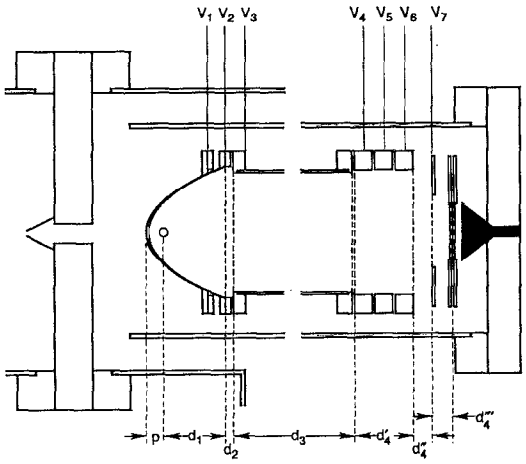

FIG. 3. Scaled drawing of the photoelectron section. Dimensions and operating voltages are given in Table I.

of the pulsed valve as shown in Fig. 2. Three stainless-steel grid plates are mounted to a circular stainless-steel disk using nylon screws. Ceramic spacers between the grid plates and the disk provide for electrical isolation of these components. The stainless-steel disk is mounted to the face of the pulsed valve using nylon screws. A teflon sheet between the disk and the pulsed valve electrically isolates the disk from the valve. The grids (Cu, 80 lines/in., 90% transmission) were attached using an Aquadaq slurry that upon drying gave reliable adhesion.

Operating conditions were optimized with the help of SIMION calculations (Fig. 2).[14] The ions are directed downward and then reflected by a reflectron to a detector at the far end of the chamber (cf. Fig. 1). The angle of the reflectron was fixed so that ions undergoing specular reflection are directed to the rear-mounted detector (R. M. Jordan, 18-mm-diam, coaxial anode, dual microchannel plate). Additional adjustments to the ion trajectories are accomplished via a set of four deflecting plates mounted to the reflectron assembly. Grounded entrance and exit grids on the deflector plate assembly minimize the penetration of the deflecting potentials outside of the assembly. The plates of the assembly are electrically isolated from one another by ceramic spacers and the entire assembly is held together using nylon screws.

At present, the ions traverse the length of the source chamber without benefit of a shielded drift tube. To reduce stray electric fields, all electrical leads in the source chamber are encased in braided copper sleeving which is tied to ground and well removed from the center of the chamber. The ion signal at the detector is amplified (Ortec 9305) and fed directly into a digital storage oscilloscope (LeCroy 9450).

C. PER/photoelectron chamber

The components of the PER/photoelectron spectrometer are illustrated in Fig. 3. Dimensions and operating voltages are summarized in Table I. The construction of the paraboloidal grid forms is described in Appendix A.

TABLE I. Dimensions and operating conditions of PER photoelectron spetrometer.

$p=1.0$ cm	$z_0=4.1$ cm	$V_1=-30$ to 0 V
$d_1=4.2$	$z_i=5.2$	$V_2=0$
$d_2=1.0$	$2x_0=8.2$	$V_3=-5$ to $+5$
$d_3=98$	$2x_i=9.2$	$V_4=+40$ typ.
$d_4'=4.2$	$2r=9.0$[a]	$V_5=-20$ typ.
$d_4''=1.3$		$V_6=+40$ typ.
$d_4'''=1.0$		$V_7=+40$ typ.

[a]Diameter of the drift tube.

The grid mesh size is 100 lines/in. and 80% transmitting. The grids are held in place by press rings (collars) as shown in Fig. 3. When stacked they are electrically isolated and separated by about 2–3 mm at the apex and less than 1 mm at the base. Because the two grids were made to the same paraboloidal equation, it was necessary to make the outer grid shorter in length to avoid contact with the inner grid. In retrospect, a slightly larger focal length for the outer grid would have given a more even spacing for the stacked grids.

The paraboloid outer circumference matches the drift-tube diameter of 9 cm. This rather large diameter was chosen (1) to allow adequate pump out of the drift tube through the grid structures, (2) to give electrons a trajectory sufficiently removed from the molecular-beam centerline to minimize scattering interactions, and (3) to achieve better field homogeneity in the paraboloidal field-free region by maximizing the ratio of total volume to fringe-field volume (Sec. III C) at the grid surface. The inner paraboloid and flat exit grid are maintained at ground potential. A negative voltage ranging from 0 to -30 V is applied to the outer paraboloid to set up a reflecting field for electrons. The optimum voltage depends on the electron energy (Sec. III C).

The molecular beam from the pulsed valve passes into the experimental chamber via a 1-mm-diam skimmer mounted to the double-sided stainless-steel flange which separates the two chambers. The molecular beam passes through holes in the apex of the PER and intersects with a laser that enters and exits through holes in the side of the PER. The intersection takes place at the focal point of the PER. We chose the direction of the molecular beam to lie along the flight-tube axis. Interference of the electrons by the molecular beam is minimized by the large paraboloid diameter, as mentioned above. Still it is advisable to ionize at the leading edge of the gas pulse and operate at moderate backing pressures. Peak broadening was evident for relatively intense gas pulse conditions. Helium has a lower collision cross section than argon and might be a better carrier gas for reducing electron-molecule scattering. However, our present use of a cryopump on the photoelectron chamber limits us to using Ar.

Reflected electrons travel the same distance to the detector along collimated paths; their kinetic energies are, therefore, measured by TOF. The flat grids separated by d_2 (Cu, 80 lines/in., 90% transmission) were attached to mounting rings using Aquadaq as explained in Sec. II B.

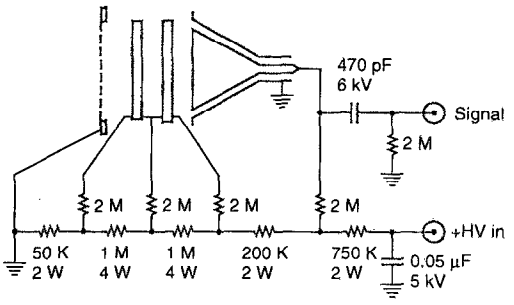

FIG. 4. Circuit for recording analog photoelectron signal from MCP. All electronics are outside of vacuum chamber.

The drift tube, and flat grid at its entrance, can be biased to accelerate electrons (positive voltage) or decelerate electrons (negative voltage) depending on experimental requirements. Accelerating electrons improves sensitivity at some expense in resolution, which is useful for detecting low-energy electrons (Sec. III A). Decelerating electrons improves resolution at some compromise in sensitivity, which is often useful for studying high-energy electrons (Sec. III B).

An einzel lens at the end of the flight tube focuses the electron distribution to match the 40-mm diameter of the detector. The lens operates using a decelerating focusing field (i.e., $V_4=V_6>V_5$). This arrangement is sensitive to the entering electron energy such that transmission diminishes rapidly in the limit of low-energy electrons and off-center trajectories (they reflect back out). To avoid this problem, electrons are accelerated by V_4 in the flat-field region between the drift tube and the einzel lens. The einzel lens was placed at the end of the drift tube instead of adjacent to the PER for two reasons: (1) to minimize focusing of direct unreflected electrons and (2) to allow electrons to travel down the drift tube without interferences that might corrupt the flight times.

The PER and drift tube are shielded from stray magnetic fields by two layers of μ metal. Sheaths of μ metal are placed around the paraboloids, around the flight tube, and at the double-sided flange separating the two chambers as shown in Fig. 1.

The detector is a 40-mm-diam dual microchannel plate (MCP) with impedence-matched coaxial anode (R. M. Jordan Co.). A high-voltage dc source supplies the necessary voltages to the plates and anode through a voltage divider network as shown in Fig. 4. High voltage is delivered into the vacuum chamber through SHV connectors and to the anode through a specially fabricated n-type connector (a Teflon insulator fills the air gap thus raising the breakdown rating to a few kilovolts). The connector shields are grounded in common with the chamber and equipment rack. Signals are capacitively decoupled from the high voltage anode as shown in Fig. 4. The recorded photoelectron signals exhibit an overshoot that recovers with a 100–200 ns time constant that tends to distort the baseline, particularly when observing weak signals that follow strong signals. We tried tuning the impedence with a cable tee (varied in length from 6 to 24 in.) that had an

adjustable resistance to ground. We also tried decoupling the high voltage provided to the plates and the anode by using separate power supplies. Neither attempt improved the overshoot. Other possible solutions not tried include floating the anode connector shield and placing the 470-pF capacitor (Fig. 4) next to the anode. One could also try using an inductively coupled output.[15]

The anode signal is boosted using a fast preamplifier (LeCroy VT120C, 350 MHz) installed directly at the signal output. Subsequent amplification is available from a rack mounted preamplifier (Stanford Research Systems SR240, 300 MHz). The amplified signals are then recorded using a digital oscilloscope (LeCroy 9450, 350-MHz bandwidth, 400-MHz sampling rate). Although the photoelectron signals are usually sufficiently strong to be detected using the analog current from the anode, it would be worth considering detection by pulse counting using a multihit time-to-amplitude converter and multichannel-analyzer system.

III. RESULTS AND APPLICATIONS

To demonstrate the applicability and improved sensitivity of the PER, we present results on CH_3I photodissociation and fragment ionization. The spectra shown here were recorded at 266 nm using 25 ps pulse durations, 20–100 μJ pulse energies, and 100–300 μm beam diameters at the molecular-beam crossing. Excitation at 266 nm leads to a direct (about 100 fs) dissociation through the repulsive $\tilde{A}$ state to CH_3 and I atom.[16] I atoms are formed in both the $^2P_{3/2}$ or $^2P_{1/2}$ spin-orbit states (henceforth, denoted I and I*, respectively). A fortuitous resonance exists for the I atom at 266 nm involving a 2+1 resonance-enhanced multiphoton ionization (REMPI).[17] It is also reported that a pseudoresonant 2+1 REMPI occurs for a CH_3 radical,[17] although the photoelectron spectra presented here indicate that this is not a major channel for CH_3^+ production. The known and proposed excitation mechanisms for 266-nm excitation of CH_3I are as follows:

$$CH_3I \xrightarrow[h\nu]{} CH_3I(\tilde{A}) \xrightarrow[100\ \text{fs}]{} CH_3(\tilde{X}^2A_2'',v)+I(5P^2P^0_{1/2,3/2}), \quad (1)$$

$$I(5P^2P^0_{3/2}) \xrightarrow[2h\nu]{} I(7P^2D^0_{5/2}) \xrightarrow[h\nu]{} I^+ + e^-, \quad (2)$$

$$CH_3(\tilde{X}^2A_2'',v) \xrightarrow[2h\nu]{} CH_3(5f^2E') \xrightarrow[h\nu]{} CH_3^+ + e^-. \quad (3)$$

The three-photon ionization of I by Eq. (2), and to a lesser extent I*, leads to production of I^+ in several J states with the ejection of corresponding energetic electrons as observed in Fig. 5. It was also the intent of this, thus far, unpublished work to obtain evidence of direct ionization through the dissociative $\tilde{A}$ state to produce parent CH_3I^+ ions. This very low-probability channel should be identifiable by a photoelectron spectrum beginning at the CH_3I ionization potential and exhibiting a Franck–Condon progression for vibrations involved in the $\tilde{A}$ state dissociative coordinate. Peaks do appear at the correct energies for the two spin-orbit states of the ground electronic state of CH_3I^+, however the expected vibrational progressions are not observed, so the assignments are tentative. Finally, if

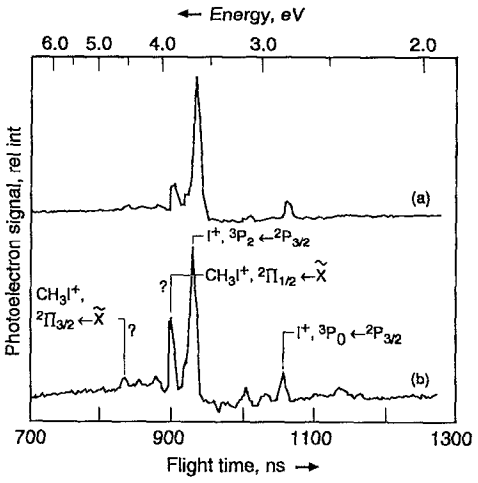

FIG. 5. Photoelectron spectra of CH_3I recorded using 25-ps, 266-nm pulses at two pulse energies and a 200-μm beam diameter: (a) 50 μJ/pulse, (b) 30 μJ/pulse. The relative intensities of individual peaks vary strongly with pulse energy. Expansion conditions were 10% CH_3I in Ar at 500 Torr backing pressure. The spectra were averaged over 2000 pulses at 10 Hz. Spectra are plotted to the same maximum intensity.

CH_3 undergoes ionization at 266 nm it is produced in much lower yield than I^+. Hence, the strong CH_3^+ signal observed in MPI mass spectra must be due to an ionization/dissociation mechanism.

A. Sensitivity

Detection efficiency is calculated by integrating over the solid angle for detection of reflected (PER) versus direct (line-of-sight) electrons for a representative distribution of electron ejection angles. The solid angle in spherical coordinates is[18]

$$d\omega = \sin\theta\, d\theta\, d\phi, \quad (4)$$

where θ is the angle measured with respect to the drift-tube axis (defined as the z axis) and ϕ is the rotation (azimuthal) angle about this axis. For axial symmetry, we integrate ϕ over 2π to obtain the solid angle between two angles θ_1 and θ_2:

$$\omega = \int d\omega = \int_0^{2\pi} d\phi \int_{\theta_1}^{\theta_2} d\theta \sin\theta$$
$$= -2\pi(\cos\theta_2 - \cos\theta_1). \quad (5)$$

Integrating over the full surface area of a sphere (i.e., θ_1, θ_2=0°, 180°) gives the expected result of 4π.

The solid angle of detection for direct electrons (line-of-sight) versus reflected electrons (PER) are calculated using the instrument dimensions in Table I. In the former case, $\theta_2 = \arctan[r/(d_1+d_2+d_3)]$, which leads to

$$(\theta_1,\theta_2) = (0°, 2.6°), \quad \omega = 4\pi(0.0010). \quad (6a)$$

The solid angle subtends about 0.1% of the surface of a sphere. For reflected electrons, $\theta_1 = \arctan(r/y_0)$, which gives

$$(\theta_1,\theta_2) = (55°, 180°), \quad \omega = 4\pi(0.79), \quad (6b)$$

TABLE II. Calculated detection efficiency of PER vs direct electron detection.

	PER	Laser polarization[a]	
		Parallel	Perpendicular
Theoretical efficiency, f[b]	off	1.5×10^{-3}	0
	on	0.27	0.82
Theoretical enhancement	off	1	0
	on	180	550
Practical enhancement[c]	off	1	0
	on	115	350
Observed enhancement	off	1	0.3
	on	28	50

[a]Relative to drift-tube axis.
[b]Calculated using Eqs. (6a) and (6c) for direct (PER=off) and reflected (PER=on) electron detection. Attenuation due to transmission through grids is not included.
[c]Includes transmission through grids; see text.

$$(\theta_1,\theta_2)=(55°,135°),\quad \omega=4\pi(0.64). \tag{6c}$$

Equation (6c) considers the possibility that a large solid angle of electrons heading toward the apex of the PER may not be reflected because of the molecular-beam entrance hole and interference with the molecular beam. Even so, the solid angle of detection of the PER is quite satisfactory.

The theoretical detection efficiency f is obtained by integrating over the solid angle of detection and the electron angular distribution $P(\theta,\phi)$:

$$f=\int_0^{2\pi} d\phi \int_{\theta_1}^{\theta_2} d\theta\, P(\theta,\phi)\sin\theta. \tag{7}$$

The electron angular distribution for angle α with respect to the laser polarization axis is given by

$$P(\alpha)=\frac{1}{4\pi}\left(1+\frac{\beta}{2}(3\cos^2\alpha-1)\right). \tag{8}$$

β values can range from $\beta=+2$ (pure $\cos^2\alpha$ distribution) to $\beta=0$ (isotropic) to $\beta=-1$ (pure $\sin^2\alpha$).[19] A value of $\beta=+2$ is assumed for ionization of I atoms by Eq. (2). The electron angular distribution for the polarized laser electric-field vector aligned parallel and perpendicular to the drift-tube z axis is given, respectively, by

$$P_z(\theta,\phi)=\frac{3}{4\pi}\cos^2\theta, \tag{9a}$$

$$P_x(\theta,\phi)=\frac{3}{4\pi}\sin^2\theta\cos^2\phi. \tag{9b}$$

Substituting Eqs. (9) into Eq. (7) lead to the functions[20]

$$f_z=\tfrac{1}{2}(\cos^3\theta_2-\cos^3\theta_1), \tag{10a}$$

$$f_x=\tfrac{1}{2}(\cos\theta_2\sin^2\theta_2-\cos\theta_1\sin^2\theta_1). \tag{10b}$$

Calculated detection efficiencies are reported in Table II.

The theoretical detection efficiencies f and enhancements do not include losses due to grid transmission. All electrons that reach the detector pass through six flat grids that each have 90% transmission. In addition, reflected electrons pass twice through the inner paraboloidal grid, undergoing a 20% minimum loss per pass (assuming 80% grid transmission for perpendicular approaches). The practical enhancements listed in Table II differ from the theoretical enhancements by the additional transmission loss due to the paraboloidal grid.

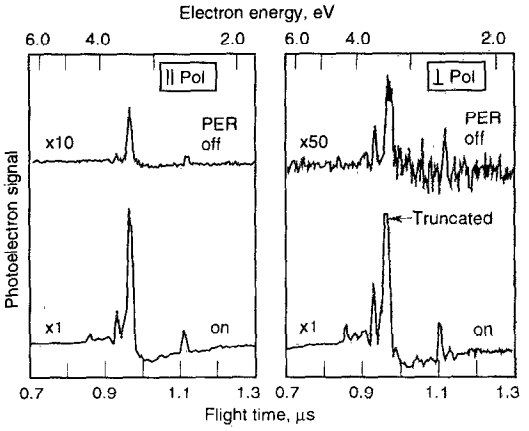

FIG. 6. Comparison of direct line-of-sight vs PER photoelectron spectra for parallel and perpendicular laser polarization. Operating conditions were $V_1=-10$ V, $V_3=0$ V. The peak marked truncated is about 50% stronger than indicated.

Direct-versus-reflected photoelectron signal intensities are measured by turning the PER on and off. For $V_1=0$, electrons pass through the PER undetected; only direct electrons are observed (Fig. 3). For $V_1<0$, the reflected electron signal overwhelms the direct electrons, which are not currently blocked. Photoelectron spectra corresponding to the PER either on or off are compared in Fig. 6 for laser polarization either parallel or perpendicular to the drift-tube axis. The relative intensities, expressed as enhancements, are reported in Table II. Although large enhancements due to the PER are observed, only qualitative agreements with calculation are obtained. We have not determined the causes of the additional losses, but we suspect a combination of at least two factors: (1) The transmission through the PER is reduced because of the large distribution of electron angles of incidence away from normal to the grid. This could conceivably reduce the signal by another factor of 2 or more. It would be worth examining whether a larger wire spacing and smaller wire diameter could be used without compromising field homogeneity and grid structure rigidity.[21] (2) The collimation of electron trajectories may be affected by distortions in the paraboloidal field and difficulty in precisely locating the focal point. For perfect collimation, the collection efficiency should be insensitive to electron energy. However, we find that applying a potential to V_3 to accelerate electrons causes an increase in signal level. The magnitude of this effect is consistent with a factor of 2–4 loss due to imperfect collimation or stray fields.

B. Resolution

The spectra in Fig. 6 indicate that energy resolution is not degraded by the PER compared to the direct electron

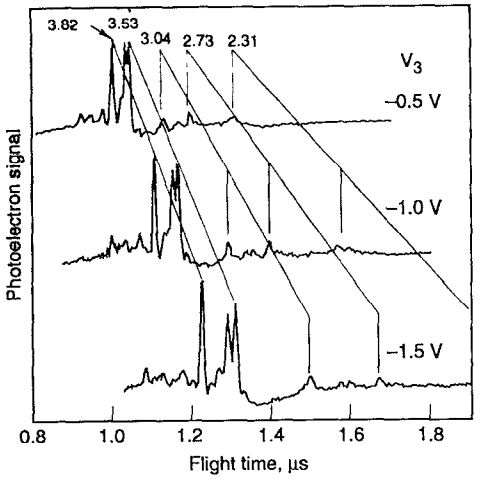

FIG. 7. Enhancement of resolution by applying negative voltage V_3 to the drift tube. Electron energies (eV) are indicated for several peaks. The spectra from top to bottom were averaged for 1800, 2000, and 4000 pulses, respectively.

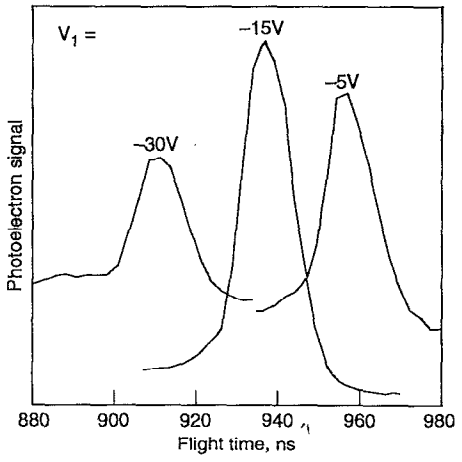

FIG. 8. Photoelectron signal vs reflection voltage for the unresolved doublet signal at 3.55 eV. Conditions were the same as in Fig. 6.

signal. Resolution is a function of the temporal width of the photoelectron peaks. The relation between electron energy E and flight time t for field-free transit to the detector is given by

$$E=\frac{m}{2}\left(\frac{l}{t}\right)^2, \tag{11}$$

where m is the electron mass and l is the transit distance. A more complicated expression results when applying fields over different regions (Appendix B), however, the above equation suffices for an estimation of resolution. Equation (11) leads to the useful expression[22]

$$\frac{\Delta E}{E}=-\frac{2\Delta t}{t}. \tag{12}$$

We obtain typical pulse widths Δt [full width half maximum (FWHM)] of 8–10 ns at about 1 μs arrival time. For the 3.82-eV signal at 910 ns, this corresponds to a resolution $\Delta E/E$ of 0.02 or 70–80 meV. For the 2.73-eV signal, the resolution is about 40–50-meV resolution.

Temporal resolution is limited largely by the combined response of the MCP, preamplifiers, and the digitizer (Sec. II C). Single electron pulse widths are about 6 ns. Hence, a factor of 2 improvement in resolution could be obtained by using faster detection electronics. Space-charge repulsion, which is evident at high laser powers, is not evident in the spectra reported here.

Resolution can be easily enhanced by retarding the electron energies in the flat-field region before entering the field-free drift tube (Fig. 3). This is illustrated in Fig. 7 for various values of V_3. The 3.55-eV signal in Fig. 6 becomes resolved into two peaks separated by about 60 meV. Resolution can be estimated by substituting $E'=E-V_3$ for E in Eqs. (11) and (12). In Fig. 7(c) resolution improves to about 30 meV for the doublet at 3.55 eV and to about 15–20 meV for the 2.73-eV signal. The signal level, however, is about a factor of 2–3 less in Fig. 7(c) than in Fig. 7(a).

C. Operating features

The photoelectron spectrometer is fairly routine to optimize. The most important adjustment is the overlap of the laser and molecular beam. The laser focal volume and photon flux are also adjusted to maximize the signal while avoiding space-charge repulsion. Final adjustments are limited to the reflector voltage V_1 and to a lesser extent the einzel lens V_4–V_6 and detector grid V_7.

An example of how a photoelectron signal varies with reflection voltage V_1 is given in Fig. 8 for the case of the 3.52-eV I-atom signal. The signal level is fairly constant over a moderately large range of voltages (typically 2–5 times the electron energy E), but loses intensity in the extremes of high and low voltage. For low reflection voltage, energetic electrons can pass through the second grid and go undetected. This occurs for electron energies $E>|V_1|/\cos\eta$, where η is the angle of incidence normal to the grid. However, some attenuation occurs even for $E<|V_1|$ (Fig. 8, $V_1=-5$ V), which may be due to electrons scattering off fringe fields at the rear grid surface. For high reflection voltage, field penetration can occur through the inner grid and cause electrons to reflect without passing through the grid.[23] Though this would decrease transmission losses, the periodicity of the field due to the wire spacing would scatter electrons and cause loss of collimation. Field penetration is evident by the direct unreflected electron arrival times, which become shorter as V_1 is increased (for example, the 3.5-eV peak arrives about 30 ns sooner for V_1 of -5 V relative to 0 V). Excessive field penetration can adversely affect signal collection in the PER mode by introducing field lines that could steer electrons away from collimated paths.

Because a detector active area that matches the drift tube cross section is not practical, we use an einzel lens at the end of the drift tube to focus the electron trajectories. This approach maximizes the detection efficiency, but

causes a slight mismatch in path lengths that can degrade resolution slightly. For example, tuning V_5 from -20 to 0 V improves temporal resolution by about 10%–20%, but decreases signal intensity by nearly a factor of 2. It is worth noting that the PER, in principle, preserves the angular distribution of the reflected electrons. However, the einzel lens as currently operated does not image this distribution very well onto the detector according to SIMION calculation.[14] Aberrations increase off axis such that the image on the detector is compressed more toward the edge. For angular distribution measurements, we would probably install a position sensitive detector that matches the drift tube diameter, thereby avoiding the need for an einzel lens.

D. Mass spectrometer

The source chamber TOF mass spectrometer in Fig. 2 (Sec. II B) was installed to allow simultaneous monitoring of mass spectra and photoelectron spectra. This capability is valuable for photoelectron studies of clusters because it enables one to know the cluster size or cluster distribution contributing to a photoelectron spectrum. Mass spectrometry is also useful for adjusting conditions (e.g., pulsed valve trigger delay and expansion conditions) for optimizing the distribution of specific cluster sizes.

The foremost design goal was to build a mass spectrometer that did not in any way compromise the performance of the photoelectron spectrometer. This required a compact ion optics assembly that mounted directly to the pulsed valve. This configuration posed several challenges: (1) it must be electrically isolated from the pulsed valve; (2) it must not disturb the expansion; (3) ions must be extracted through a relatively dense gas jet; and (4) ions must be steered to the back of the chamber.

The grids had to be operated at low voltage for two reasons: (1) to avoid dielectric breakdown through or around the insulator, and (2) to minimize the effect of the grounded pulsed valve on the accelerated ion trajectories. Suitable operating conditions were identified by SIMION calculations (Fig. 2). The ion optics assembly does not appear to disturb the free-jet expansion. We have recorded photoelectron spectra of CH_3I with and without the ion optics assembly installed and observe no significant differences in performances. We have also recorded photoelectron spectra for large clusters indicating that cluster formation is not impeded by the ion optics assembly.

The problem of extracting ions through the gas jet can be severe. We managed to obtain a strong signal and well-resolved mass spectra for CH_3I ionization, as shown in Fig. 9. However, we had much more difficulty achieving useful mass resolution for clusters [both $(CH_3I)_n$ and phenol-$(NH_3)_n$]. We suspect that the mass resolution deteriorates with increasing collision cross section of the ion. There are a number of means for obtaining satisfactory mass spectra: reducing backing pressure, ionizing at the extreme leading edge of the gas pulse, and ionizing as far downstream and off the free-jet centerline as possible. However, these conditions are not representative of the optimum beam conditions or beam composition for recording photoelectron spectra. Although the mass spectrometer is useful for independent experiments, it is currently of limited utility as a real-time beam diagnostic for photoelectron spectroscopy. An alternative approach we are exploring for obtaining simultaneous mass and electron TOF spectra is a photoelectron-photoion coincidence experiment using a high repetition rate mode-locked laser (cf. Sec. IV).

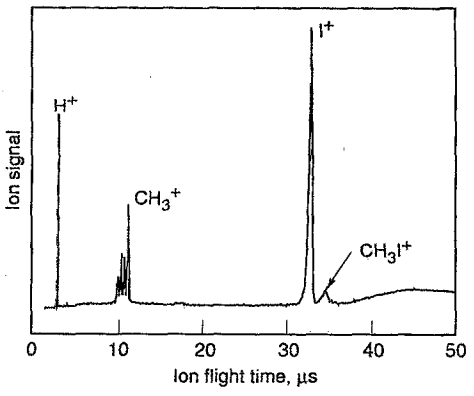

FIG. 9. CH_3I mass spectrum recorded using the source-chamber ion optics/reflectron assembly.

E. Remaining issues

Photoelectron ejection from grids: Significant electron signal arises from the grids, even though we use an aperture and lens to clean up and focus the laser beam that passes through the PER region. Electrons that are photoejected from the outer grid are identifiable by their appearance in TOF spectra at an energy corresponding to the reflection voltage V_1.[24] (Presumably electrons are also ejected from the inner grid, but they are not apparent in the TOF spectra because of their low energy.) Because V_1 is typically set at about twice the maximum electron energy (cf. Sec. III C), the scattered electron signal appears at a much earlier time than the photoelectron signals of interest. However, in experiments involving very weak photoelectron signals, the scattered electron signal can be significantly stronger and impart a baseline distortion on subsequent signals. One solution is to place deflector plates near the detector that can be pulsed on to reject the scattered signal. In some situations, the scattered electron signal can be useful. Because the electron energy is equivalent to V_1, the flight time as a function of V_1 gives a quick determination of the energy scale for a TOF spectrum.

Transmission and other losses: Electrons must pass through several grids, which limits the transmission of the spectrometer. The maximum transmission probability, based on six flat grids (90% transmission) and the inner paraboloidal grid (80% transmission), is 34%, As discussed earlier (Sec. III A), this figure is likely to be much less because the transmission through the paraboloidal grids is reduced for electron angles of incidence away from normal. Possible solutions include matching the flight-tube and detector diameters (see below) to eliminate the need

for the einzel lens and acceleration grids, and by using thinner and wider spaced wires for the inner paraboloid.[21]

Molecular-beam axis: Although our choice of a coincident molecular-beam/flight-tube axis works successfully, there are arguments in favor of a perpendicular arrangement. This would reduce the pumping requirement of the drift tube and the need to have electron trajectories far removed from the molecular-beam centerline. The drift-tube diameter could then be made smaller to match the detector diameter, thus eliminating the need for an einzel lens. This situation would improve electron transmission and imaging. However, a perpendicular arrangement requires a well-collimated molecular beam to avoid scattering off the exit hole and preferably a differentially pumped molecular-beam catch to keep the pressure low in the flight-tube chamber. It also requires four holes rather than three in the PER, which might lead to increased losses and additional stray fields.

IV. DISCUSSION

The PER design of Trevor *et al.*, adapted for molecular-beam use, provides a significant enhancement in detection efficiency over standard line-of-sight TOF photoelectron spectroscopy. The design suggests a number of powerful applications. The ability to image the electron distribution on a position-sensitive detector has already been described as a method of measuring the electron angular dependence.[2]

We are exploring two other applications of the PER for molecular-beam ionization. The first is a time-resolved photoelectron/photoion coincidence spectrometer (PEPICO)[25] using a high repetition rate mode-locked laser. Our interest lies in measuring dynamical properties of clusters by detecting the time dependence of the photoelectron spectrum for specific cluster sizes. The proposed method is able to resolve different cluster sizes even when they have overlapping excited-state and/or photoelectron spectra. The use of a high collection efficiency electron energy analyzer is important for a PEPICO experiment. To ensure a true ion/electron coincidence, the probability of an ionization event per laser pulse must be very low, which reduces count rate. The experiment can suffer considerably further if the probability of detecting the electron is also very low. Recently, Rademann *et al.* reported on a PEPICO device incorporating a magnetic bottle electron energy analyzer.[26]

A second promising application is to use the PER as a positive-ion kinetic energy analyzer. The kinetic energy of an ion fragment or of a neutral fragment that is subsequently ionized can be measured with high sensitivity and energy resolution. Furthermore, the ability to simultaneously image the angular distribution of a photofragment enables one to measure angular-velocity distributions (i.e., two-dimensional kinetic energy distributions) on a single-shot basis.

ACKNOWLEDGMENTS

We benefitted from the generous help of many people. We are grateful to Dr. D. J. Trevor for many valuable conversations, to Dr. S. Allendorf for sharing information on their spectrometer design, and to Dr. J. E. Pollard for innumerable discussions on instrument design.

APPENDIX

A. Fabrication of the paraboloidal grids

The grids were constructed as follows. Two lexan forms were machined according to the formula $x^2=4pz$ ($p=1.02$ cm). The forms for the inner and outer grids were fabricated with base diameters of 9.2 and 8.2 cm, respectively. The bases were extended cylindrically by 0.5 cm to permit attachment of the clamping collars. For convenience of assembly, the forms were secured by a post screwed into the center of the base. Holes were drilled into the forms as guides for cutting the molecular-beam entrance hole and the laser entrance and exit holes. Stainless-steel collars were fabricated [0.125-in. thickness, 4.5-in. outer diameter (o.d.)] to hold the grid material in place. The inner diameter (i.d.) of the inner collars (away from the base) of both grids were beveled to lie flush with the forms (cf. Fig. 3), although this feature may be unimportant. The i.d. of the outer collars are 4.125 in. The outer collars were attached to the side of the forms by four screws.

Stainless-steel mesh (100×100 lines/in., 0.001-in. wire diameter, 80% transmission) was stretched over the lexan forms and secured in place by clamping the inner collar to the outer collar by eight screws. The i.d. of the outer collar exceeds that of the paraboloid base in order to leave a section of grid material exposed for hardening. This lip allows the final paraboloidal grids to be securely mounted in the spectrometer. The hardening procedure begins by immersing the assemblies in DS9, a stainless-steel brightening/etching solution. The etching process was monitored at frequent intervals by removing the forms, gently rinsing them in a water bath, and determining the wire diameter using a microscope equipped with a graticule. A reduced wire diameter of 0.0006 in. was reached in about 4–6 min, depending on solution conditions (temperature, concentration, age). We initially attemped to reduce the wire diameter by electropolishing according to the procedure by TVF.[2] However, we were unsuccessful in obtaining uniform results across the entire grid surface.

The chemically etched grids were then plated by immersing the assemblies in an electrodeless nickel plating solution. As with the etching process, the plating process was monitored closely by removing the forms, rinsing them thoroughly in a water bath, and using the graticuled microscope to determine the wire diameter. The wire diameter was brought up to the original 0.001-in. value corresponding to an 80% transmission for the final nickel-plated paraboloidal grids. The nickel plating achieves structural rigidity by locking the grid wires at the junctions. Also, the greater hardness of nickel relative to stainless steel contributes to the stiffness. Chromium plating, in principle, is

preferable because of its lower magnetism compared to nickel. However, we had difficulty finding a local company with the facilities for chemically plating chromium. It is worth noting that our nickel-plated grids do not adversely affect energy resolution. Perhaps the amorphous state of the plated nickel minimizes magnetic effects. We did not attempt the method of electroplating by TVF because of the difficulty we experienced in electropolishing mentioned above.

Holes for the molecular beam and laser were cut into the nickel-plated grids using the 532-nm focused output of a Nd:YAG laser. The grid assemblies were mounted on a two-axis translation stage and the guide holes in the lexan forms, described above, were used to outline the desired 1-cm holes. This procedure was very effective at cutting the holes without making physical contact that might deform the paraboloidal shapes.

The grids were gently removed from the paraboloidal forms taking care not to allow creases or dimples to occur. The outer collar was replaced with a similar collar, but with an i.d. that matched that of the paraboloidal base. This secured the nickel plated lip of the paraboloids for final assembly in the spectrometer. The grids were attached to the flight tube using stainless screws through ceramic sleeves for electrical isolation. Ceramic spacers were also used to separate the grid mounting collars and the flight-tube end flange (cf. Fig. 3).

B. Calibration of energy scale

The transformation of electron flight time to initial kinetic energy E is accomplished by calculating the transit times for each stage of the spectrometer (cf. Fig. 3, Table I). The equations for distance and velocity as a function of time t are

$$s=s_0+v_0t+\frac{q\mathscr{E}t^2}{2m}, \tag{B1}$$

$$v=v_0+\frac{q\mathscr{E}t}{m}, \tag{B2}$$

where v_0 is initial velocity, $\mathscr{E}$ is the electric field, and q and m are the electron charge and mass. The product $q\mathscr{E}$ is a positive quantity for an acceleration field. The transit time through each stage follows from Eq. (B1):

$$t=\frac{-v_0+(v_0^2+2q\mathscr{E}d/m)^{1/2}}{q\mathscr{E}/m} \quad (\mathscr{E}\neq 0)$$

$$=d/v_0 \quad (\mathscr{E}=0), \tag{B3}$$

where s_0-s is the length d of each stage.

We define four major stages to our photoelectron spectrometer (Fig. 3, Table I): the PER ($d=d_1+2p$), the accelerator (d_2), the drift tube (d_3), and the einzel lens assembly ($d_4'+d_4''+d_4'''$). The transit time in the reflecting region of the paraboloidal grids is insignificant as discussed by TVF, and ignored in this treatment. The preacceleration region, einzel lens d_4', and post-drift region $d_4''+d_4'''$ involve complicated trajectories. We therefore treat these regions as a single stage of distance d_4 and *effective* field $\mathscr{E}_4$. This approximation is acceptable because the transit time through this region is very small relative to the total flight time (typically $<2\%$).

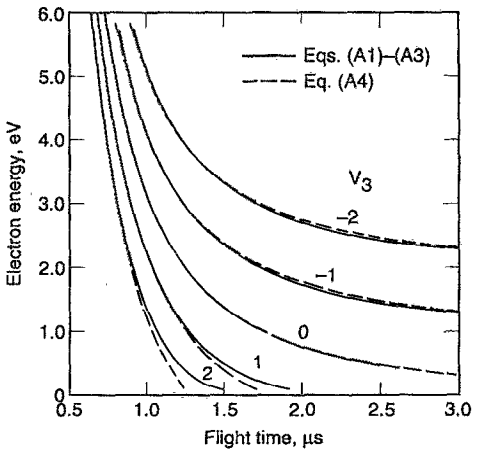

FIG. 10. Calculated relationship between electron energy E and flight time by a multistage calculation using Eqs. (B1)–(B3) and by an approximate calculation using Eq. (B4). The latter calculation uses values of d_e ranging from 103 to 107 cm in integral increments for V_3 values of -2 to $+2$ V, respectively.

Calculated flight times were calibrated to the I atom and other assigned signals in Fig. 5 using a fitting routine involving Eqs. (B1)–(B3). Only d_3 and $\mathscr{E}_4$ were adjusted to obtain a good fit. Excellent fits were obtained for 96 cm and 10 V/cm, respectively, which compare well to the actual instrument values in Table I. Calculated plots of E vs total t for various values of V_3 are given in Fig. 10. These results agree very well with observed spectra over a wide range of E and V_3. The transit time in d_3 usually dominates the total flight time (typically 90%), which makes possible an approximate expression for relating E from t:

$$E=\frac{md_e^2}{2t^2}-V_3, \tag{B4}$$

where d_e is an *effective* length obtained by fitting Eq. (B4) to the calculated curves in Fig. 10. Good agreement with the multistage calculation above is obtained for a wide range of conditions; the simple expression deviates as the transit time through the drift tube becomes a decreasing fraction of the total flight time.

The photoelectron spectra presented in this paper are plotted linearly in time, which tends to deemphasize the intensity of low-energy peaks. According to Eq. (12), peaks corresponding to decreasing E that have a constant ΔE would appear with an increasing Δt width. The intensities $I(E)$ on a linear energy scale should be scaled to preserve the peak area for a time-domain intensity $I(t)$ (i.e., Jacobian transformation). This gives

$$I(E)=I(t)\Delta t/\Delta E. \tag{B5}$$

From Eq. (12) and the relation $E\propto 1/t^2$, it follows that

$$I(E)\propto I(t)t^3. \tag{B6}$$

[1] K. Kimura, Adv. Chem. Phys. **60**, 161 (1985).
[2] D. J. Trevor, L. D. Van Woerkom, and R. R. Freeman, Rev. Sci. Instrum. **60**, 1051 (1989).
[3] G. Liu, J. J. Barton, C. C. Bahr, and D. A. Shirley, Nucl. Instrum. Methods A **246**, 504 (1986).
[4] P. Kruit and F. H. Read, J. Phys. E **16**, 313 (1983).
[5] K. Müller-Dethlefs and E. W. Schlag, Ann. Rev. Phys. Chem. **42**, 109 (1991).
[6] J. A. Syage and J. Steadman, J. Phys. Chem. **96**, 9606 (1992).
[7] J. A. Syage, Chem. Phys. Lett. **202**, 227 (1993).
[8] J. M. Smith, C. Lakshminarayan, and J. L. Knee, J. Chem. Phys. **93**, 4475 (1990); J. M. Smith, X. Zhang, and J. L. Knee, *ibid.* **99**, 2550 (1993).
[9] X. Song, C. W. Wilkerson, Jr., J. Lucia, S. Pauls, and J. P. Reilly, Chem. Phys. Lett. **174**, 377 (1990).
[10] B. Kim, N. Thantu, and P. M. Weber, J. Chem. Phys. **97**, 5384 (1992).
[11] T. Baumert, C. Röttgermann, C. Rothenfusser, R. Thalweiser, V. Weiss, and G. Gerber, Phys. Rev. Lett. **69**, 1512 (1992).
[12] K. Kimura, K. Sato, K. Okuyama, and M. Takahashi, in *Ultrafast Phenomena 6*, edited by T. Yajima, K. Yoshihara, C. B. Harris, and S. Shionoya (Springer, Berlin, 1988), p. 483.
[13] E. W. Fournier, R. A. Hertz, J. Steadman, R. B. Cohen, and J. A. Syage, Appl. Spectrosc. **45**, 468 (1991); J. A. Syage, P. M. Felker, and A. H. Zewail, J. Chem. Phys. **81**, 2233 (1984).
[14] D. A. Dahl and J. E. Delmore, *The Simion PC/PS2 User's Manual, Ver 4.0* (EG&G Idaho National Engineering Laboratory, Report No. EGG-CS-7233, Rev. 2, April 1988).
[15] M. G. White, R. A. Rosenberg, G. Gabor, E. D. Poliakoff, G. Thorton, S. H. Southworth, and D. A. Shirley, Rev. Sci. Instrum. **50**, 1268 (1979).
[16] J. L. Knee, L. R. Khundkar, and A. H. Zewail, J. Chem. Phys. **83**, 1996 (1985); G. N. A. van Veen, T. Baller, and A. E. de Vries, Chem. Phys. **97**, 179 (1985); J. F. Black and I. Powis, *ibid.* **125**, 375 (1988).
[17] Y. Jiang, M. R. Giorgi-Arnazzi, and R. B. Bernstein, Chem. Phys. **106**, 171 (1986).
[18] W. J. Moore, *Physical Chemistry*, 4th ed. (Prentice-Hall, Englewood Cliffs, NJ, 1972), p. 130ff.
[19] J. Berkowitz, *Photoabsorption, Photoionization, and Photoelectron Spectroscopy* (Academic, New York, 1979), p. 358ff.
[20] $P_y(\theta,\phi)=\sin^2\theta\sin^2\phi$, however, the integration by Eq. (7) leads to $f_y=f_x$ as expected.
[21] A weave grid as opposed to straight-wire mesh is more easily stretched over the paraboloidal forms and allows the wire spacing to be varied by the stretching tension. (R. E. Continetti, private communication).
[22] Resolution is also affected by the variation in turnaround time in the reflecting region and by mismatches in path length Δl due in part to the finite size of the ionization volume. TVF (Ref. 2) showed that the former factor is insignificant. Length mismatches due to laser focal volumes are also minimal (laser beam diameters less than 1 mm).
[23] Field penetration creates an effective voltage different from the nominal voltage. Based on SIMION calculations, the penetration of a field of magnitude $\mathscr{E}$ to a depth equal to the grid spacing s creates a voltage change of approximately $\mathscr{E}s/10$.
[24] The scattered electrons should be accelerated normal to the paraboloid surface, so it is unclear how they reach the detector with relatively narrow flight-time distributions. Presumably only a small fraction of these electrons are reaching the detector.
[25] T. Baer, in *Gas Phase Ion Chemistry* (Academic, New York, 1984), Vol. 1, p. 153.
[26] K. Rademann, T. Rech, B. Kaiser, U. Even, and F. Hensel, Rev. Sci. Instrum. **62**, 1932 (1991).